From soap-film packed droplets to multilayer antibubbles: Formation and stability

Cyril André,[1,*] Cyriaque Amerein,[2] Jonas Miguet,[3] Benoit Scheid,[3] and Stéphane Dorbolo[1]

[1] *PtYX, CESAM, Université de Liège, B-4000, Liège, Belgium*
[2] *Physics Department, École Normale Supérieure, F-75230, Paris, France*
[3] *TIPs, École de Bioingénierie de Bruxelles, B-1050 Bruxelles, Belgium*

An antibubble is an object in which a liquid core is separated from a surrounding liquid by a thin spherical gas shell. Such structures can be generated when a droplet crosses a soap film with sufficient kinetic energy to become wrapped by the film, which then merges upon contact with a liquid bath. When droplets fall through multiple soap films, multilayer antibubbles can be generated. In this paper, the conditions required to successfully generate monolayer and multilayer packed droplets are studied in order to optimize the formation of monolayer and multilayer antibubbles. In particular, the geometrical factors and the composition of the liquid that makes up both the droplets and the soap films are discussed. The stability of antibubbles generated using this method is also investigated as a first case study. The robust formation of monolayer and multilayer antibubbles is a key to open opportunities in drug delivery without the use of either oil or solid compounds. Moreover, this method allows for the production of monodisperse, millimetric, and multilayered antibubbles.

I. INTRODUCTION

Antibubbles are unusual structures in which a liquid core, of millimetric dimension, is separated from the rest of the liquid bulk by a micrometric layer of gas, usually composed of air. It can be seen as the opposite of a soap bubble in the sense that the liquid and gas are inverted, hence the name. These "inverted bubbles" were first reported by Hughes and Hughes in 1932 [1], and named "antibubbles" in 1966 by Pavlov-Verevkin [2]. The thin air layer constituting antibubbles holds promise for various applications, such as controlled drug delivery to specific locations, as antibubbles are very responsive to ultrasound [3] or magnetic fields when using a ferrofluid in the core [4], or enhanced liquid-gas mass transfer given the very high surface-to-volume ratio of the embarked gas [5].

Several methods to generate antibubbles have been developed in recent years [6]. One of them consists of gently pouring a soapy liquid into same liquid. The incoming liquid jet entrains air below the surface of the bath, entrapping air and eventually forming antibubbles [7–9]. Other methods exist, for example, through droplet impact on a soapy solution [10], bubble coalescence [11], or with a two-step process involving water-oil-water emulsions [12].

In this paper, we investigate a method that involves the passage of a droplet, composed of a concentrated surfactant solution, through one or several soap films. This system can be characterized by the geometry, surface tension, viscosity, and density of both droplet and soap films. An optimal velocity exists at which the droplet deforms the soap film without breaking it. This interaction results in a topological transition: the film wraps the droplet by a thin liquid layer and subsequently recovers its original shape. The resulting object, referred to as a packed droplet, has been the subject of many investigations [13–19]. The packing process, also called an encapsulation process, is governed by the ratio of the droplet's inertial energy to the surface energy associated with the film deformation. Consequently, the packing can be characterized using the Weber number, calculated at the moment of crossing, which is defined as

$$\mathrm{We} = \frac{\rho U^2 D}{\gamma}, \tag{1}$$

where U is the speed of the falling droplet, D is the droplet diameter, ρ and γ are the density and surface tension of the liquid, respectively. In previous studies, packing was found to occur in two Weber regimes ranging from about 20 to 80 and from about 200 to 500 [17–19].

When a liquid bath is placed beneath the soap film, the packed droplet eventually impacts the interface. At low speeds, as discussed in this study, the outermost layer merges with the bath, leaving a spherical air layer and forming an antibubble [20]. Using multiple soap films allows for the formation of several liquid layers, and consequently multiple gas layers around the droplet, resulting in a multipacked droplet. Similarly to the packed droplet, upon impact with the liquid pool, the outermost layer of a multipacked droplet may merge with the pool, leaving several air layers separated by liquid layers, thus forming a multilayer antibubble. Previous studies have detailed the control parameters needed to form a single layer around a falling droplet [20–22], but the parameters for the formation of a multilayer droplet and subsequent conversion into a multilayer antibubble, though reported in [20], have not been systematically investigated yet.

The aim of this paper is to determine the optimal parameters for the generation of these structures. We investigate the interaction between the droplet and the film, focusing on encapsulation dynamics and the kinetic energy loss of the droplet during this process. We experimentally explore the parameters governing the formation of single- and multipacked droplets, including impact velocity and viscosity. Finally, we examine the conversion

* cyril.andre@uliege.be

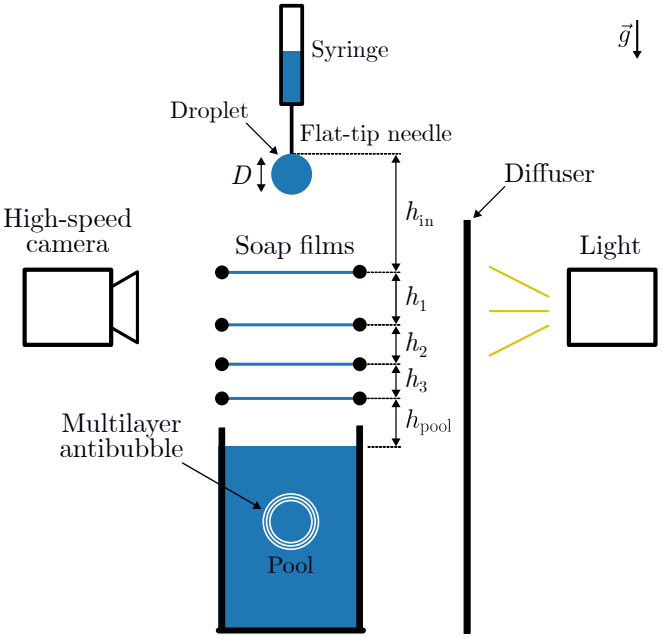

FIG. 1. Sketch of the experimental setup for generating multilayer antibubbles. In all experiments, the droplet and the soap films were composed of the same solution. The bath always contains the base solution, except when studying the lifetime of antibubbles.

of a (multi-)packed droplet into an antibubble with one or several layers, including a first study of the lifetime of such objects.

II. EXPERIMENTAL SETUP

The experimental setup is presented in Fig. 1. A height-adjustable syringe allows the release of a droplet at a controlled height h_{in} from the first soap film. The distance between the soap film number i and the soap film $i+1$ is noted h_i. The final film was placed at a distance h_{pool} from the interface of the liquid pool. The setup was illuminated with a high-intensity light source diffused by a semi-transparent PMMA panel. Falling droplets were recorded using a high-speed camera (Phantom MIRO 310) equipped with a Nikon Macro 100 mm f/2.8 lens. The camera resolution was set to 1280×300 pixels, the frame rate to 8500 frames per second, and the exposure time to 30 µs. The spatial calibration (m/px) depended on the specific experimental configuration and was determined from a reference length in the field of view for each case.

The droplets, soap films, and pool were all composed of a solution of bidistilled water mixed with the commercial dish soap Dreft [23]. This commercial soap contains some traces of ethanol and three surfactants: an anionic one, sodium lauryl ether sulfate; a zwitterionic one, lauryldimethylamine oxide; and a non-ionic one, fatty alcohol ethoxylate.

Glycerol (wt%)	γ (mN/m)	μ (mPa.s)	ρ (kg/m^3)
0	25.8	1.0	998
30	25.6	2.5	1075
50	24.4	6.0	1123

TABLE I. Physical properties of the working solutions. Accuracy for γ is $\pm$ 0.5 mN/m, for μ is $\pm$ 0.5 mPa.s and for ρ is $\pm$ 2 kg/m^3.

The surface tension γ of the Dreft solutions was measured for various concentrations using the pendant drop method [24]. The results are shown in the Supplemental Material [25]. The surfactant concentration of the solutions used in this work was fixed at 5 wt.%, which corresponds approximately to 25 times the critical micelle concentration, above which surface tension is rather independent of the concentration.

The viscosity of the soapy solutions was tuned by changing the proportion of glycerol by weight (0 wt%, 30 wt%, and 50 wt%). In total, three working solutions were used: (i) 95 wt% of water and 5 wt% of soap, (ii) 65 wt% of water, 5 wt% of soap and 30 wt% of glycerol, (iii) 45 wt% of water, 5 wt% of soap, and 50 wt% of glycerol. Physical properties of these working solutions are summarized in Table I. The density ρ was obtained by measuring the mass of a volume of 100 ± 0.2 mL of the liquid. The surface tension was measured by analyzing the oscillation frequency f_2 of the second mode of a free-falling droplet and using the relation $\gamma = \pi^2 \rho D^3 f_2^2/16$, with D the droplet diameter [16]. The values are reported in the table and results from the average over five measurements. The surface tension of the pure soap-water solution is satisfactorily compared with the one measured by the pendant drop method, thus validating this approach for the determination of surface tension under our working conditions [25]. The viscosity of the different solutions has been assumed to be close to the water-glycerol mixture and their values were taken directly from the literature [26]. The laboratory temperature was 20.0 ± 0.5 °C and was considered stable and thus not affecting the physical properties of the solutions.

Soap films were formed by immersing a 19 mm diameter polypropylene (PP) ring in a soap-water solution and then slowly lifting it. The ring, repurposed from a commercial bubble wand toy, was mounted horizontally. Once formed, the films were prepared by passing ten droplets through them from a fixed distance. These impacts caused the soap films to thin and become more homogeneous, as observed optically by examining the interference fringes. The ring remained stable during the experiments, showing no significant motion during droplet impacts using high-speed imaging. Although quantitative angular measurements were not performed, visual inspection indicated only a very slight deviation from horizontality. Film thicknesses were estimated by puncturing the films with a dry needle. By assuming a balance between the surface and inertial forces, the retraction speed of the thin film was compared to the Taylor-Culick speed,

$v_{TC} = \sqrt{2\gamma/\rho\delta}$, from which the thickness δ of the film was determined [27, 28]. Ten films were tested for the solution without glycerol: thicknesses ranged from 1.8 µm to 2.9 µm, with an average of 2.3 µm. For the two other solutions, *i.e.* with glycerol, this method fails due to their higher viscosities [29, 30].

Droplets were generated by pinching off a soap-water solution from the end of a flat-tipped needle, with needle outer diameters ranging from 0.32 mm to 4 mm. This range allowed for the formation of droplets with diameters ranging from 1.68 mm to 3.37 mm with a standard deviation of ±0.05 mm.

Note that in experiments, droplets and films were always of the same composition, *i.e.* both contain the same amounts of glycerol. When measuring the probability of antibubble formation, the bath was prepared from a solution free of glycerol. When measuring antibubble lifetimes, the bath was prepared from a solution containing 50 wt% of glycerol.

To analyze the data, we extracted the diameter and speed of the droplets using video analysis using Python and OpenCV. Assuming an elliptical shape for the droplet, the average diameter D is given by $D = \sqrt[3]{D_z D_{xy}^2}$, where D_z and D_{xy} are the diameters along the falling axis and its normal plane, respectively.

III. RESULTS

A. Film-droplet interaction

When a droplet passes through a soap film, the film deforms and can wrap it [16], resulting in the formation of a "packed droplet", also referred to as an "encapsulated droplet". This section presents a general characterization of the interaction between a soap film and a droplet passing through it, regardless of whether encapsulation occurs or not.

Assuming the droplet is in free fall, its impact velocity on the thin film is given by $U = \sqrt{2gh_{\text{in}}}$, where h_{in} represents the falling height. Using this expression, the droplet's Weber number, defined in Eq. 1, can be rewritten as

$$\text{We} = \frac{2\rho g D}{\gamma} h_{\text{in}} = A_{th} h_{\text{in}}, \tag{2}$$

where $A_{th} = 2\rho g D/\gamma$ represents the increase in the Weber number per unit of falling distance. This rewrite highlights that the droplet Weber number can be controlled directly by varying the falling height. However, a more accurate experimental determination is obtained by substituting the speed of the droplet center of mass into Eq. 1. To extract this speed, the vertical trajectory is obtained from image analysis. The trajectory is fitted with a second-degree polynomial, and the instantaneous speed at the film crossing is determined by differentiating the fit at that moment. The Weber number values reported in this study were computed using this method.

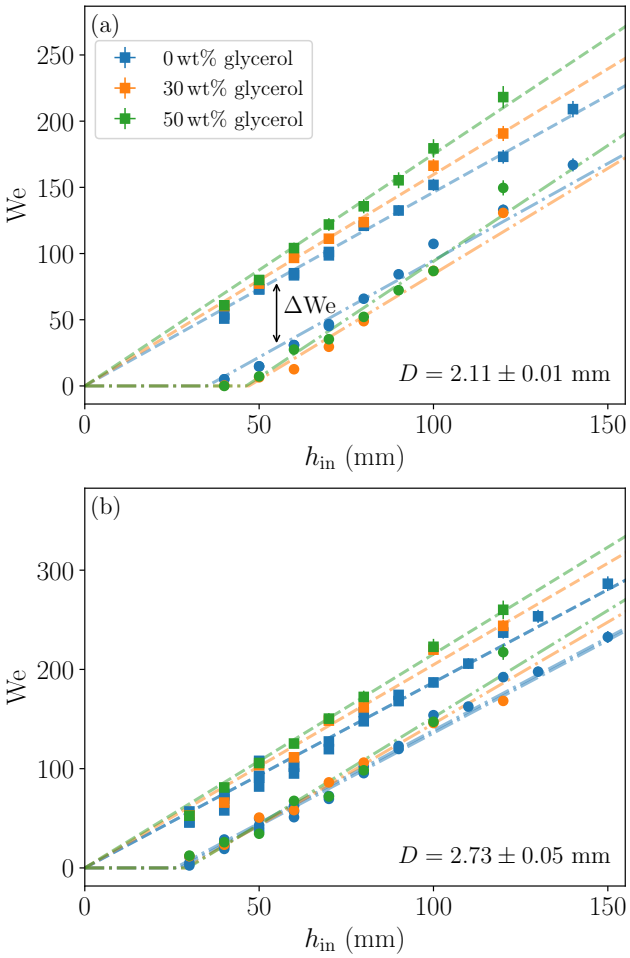

FIG. 2. Droplets' Weber numbers We_{in} before (squares) and We_{out} after (circles) that the droplets cross the soap film, for three solutions and two droplet diameters: (a) $D = 2.11 \pm 0.01$ mm and (b) $D = 2.73 \pm 0.05$ mm. Dashed and dash-dotted lines are linear fits for We_{in} and We_{out}, respectively, and ΔWe is the difference between both.

Because of the interaction between the droplet and the film, the crossing results in an energy cost for the droplet: the droplet is slowed down, leading to a decrease of the Weber number after the crossing. The Weber numbers before crossing the film, We_{in} (squares), and after, We_{out} (circles), are presented as functions of the falling height h_{in} for two different droplet diameters, $D = 2.11 \pm 0.01$ mm and $D = 2.73 \pm 0.05$ mm, in Fig. 2. Each point corresponds to the mean of 7-10 droplets. Results are reported for the three viscosities associated with the three working solutions. The dashed and dash-dotted lines represent the fits of the relations $\text{We}_{\text{in}} = Ah_{\text{in}}$ and $\text{We}_{\text{out}} = \max(0, Ah_{\text{in}} + B)$, respectively, where A and B are the fitting parameters. As shown in Fig. 2, both We_{in} and We_{out} increase linearly with the falling height, in agreement with Eq. 2. This linear dependence reflects the direct conversion of the gravitational potential energy

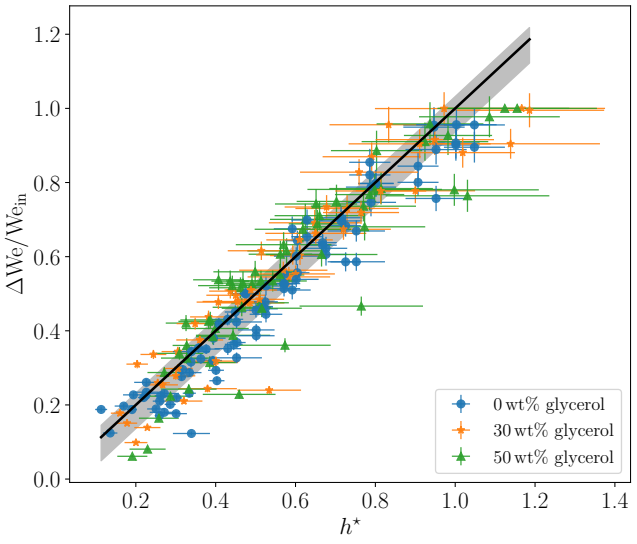

FIG. 3. Dependency of the relative loss $\Delta\mathrm{We}/\mathrm{We}_{\mathrm{in}}$ as a function of the dimensionless height $h^\star = h_c/h$ for three solutions and for droplet diameters ranging from 1.70 mm to 3.34 mm. The solid black line corresponds to the theoretical prediction with unit slope. The shaded gray region indicates the empirical asymmetric dispersion of the experimental data around this prediction.

into the kinetic energy of the droplet, while the offset B captures the energy loss associated with the interaction with the soap film. The preservation of the linearity after crossing suggests that the film primarily acts as a dissipative element, rather than fundamentally altering the droplet dynamics and associated law. Indeed, the Weber loss $\Delta\mathrm{We} = \mathrm{We}_{\mathrm{in}} - \mathrm{We}_{\mathrm{out}}$ is, at leading order, constant for a given diameter, which confirms the role of the soap film acting as a dissipative element. In summary, the parameter B represents the Weber loss $\Delta\mathrm{We}$ during crossing and is found to be in the range of $[40, 70]$, depending on the droplet diameter.

The values of A_{th}, A, B, and $-B/A$ are reported in Table II for the two droplet diameters and the three solutions presented in this section. The effect of the droplet size is clearly visible for A_{th}, A and the ratio $-B/A$, confirming that the critical conditions required for the film crossing depend on the droplet size, as expected. In contrast, the parameter B remains nearly constant between diameters, indicating that energy dissipation is size-independent within the explored range. Regarding the effect of viscosity, no measurable variations can be identified since standard deviation overlaps, suggesting that the crossing dynamics do not depend significantly on the viscosity of the soap film, which is consistent with previous observations for rigid spheres [22].

To characterize the Weber loss, the relative Weber loss for each data point can be defined as

$$\frac{\Delta\mathrm{We}}{\mathrm{We}_{\mathrm{in}}} = \frac{\mathrm{We}_{\mathrm{in}} - \mathrm{We}_{\mathrm{out}}}{\mathrm{We}_{\mathrm{in}}}\,. \tag{3}$$

In addition, for each diameter and solution, it is possible to define a critical height h_c corresponding to the minimal height needed to cross the film. In order to compute this value for all droplet diameters and solutions, we used the data plotted in the Fig. 2 and assumed the minimum height required to cross the film corresponds to the abscissa of the linear fit $Ah_{in} + B$ when $\mathrm{We}_{\mathrm{out}} = 0$, *i.e.*, $h_c = -B/A$. We then find that the critical heights for the glycerol-free solution are 35.14 ± 1.44 mm and 26.85 ± 0.79 mm for $D = 2.11 \pm 0.01$ mm and $D = 2.73 \pm 0.05$ mm, respectively. Now, relying on the constancy of $\Delta\mathrm{We}$ and the experimental observation that $\mathrm{We}_{\mathrm{out}}$ cancels out when $h_{\mathrm{in}} = h_c$, we can predict that the energy loss scale as $\Delta\mathrm{We}/\mathrm{We}_{\mathrm{in}} = h^\star$, where we define $h^\star = h_c/h$, *i.e.*, the inverse of the falling height normalized by the critical height. This prediction is presented in Fig. 3 for the three solutions described in Table I and droplet diameters ranging from 1.70 mm to 3.34 mm. The theoretical prediction, corresponding to a line of unit slope, is shown as a solid black line, while the asymmetric dispersion of the data around this prediction is represented by the shaded gray areas. The limited spread of the data around the theoretical line underlines the non-measurable dependence of the energy cost of the crossing on the viscosity of the film, as discussed in literature [22]. This conclusion is further supported by the values reported in the column B of Table II, as discussed above.

Regarding a purely energetic argument, the energy of the droplet has to be large enough to overcome the deformation energy of the soap film. This has been described in the literature for rigid sphere [22] and can be adapted to the present experiment. By assuming the deformed cavity of the soap film to be a vertical cylinder of radius $R = D/2$, which correspond to the droplet radius, and length $L \approx 6R$, as found empirically by Le Goff et al. [22], the deformation energy is given by $E_{\mathrm{s}} \approx 24\pi R^2\gamma$ when considering that two interfaces are created. Balancing this energy with the energy of the droplet at the moment of the crossing, $\frac{4}{3}\pi R^3\rho g h_c$, gives

$$h_c \approx \frac{18\gamma}{\rho g R}, \tag{4}$$

which gives $h_c = 43$ mm and 34 mm for $D = 2.11 \pm 0.01$ mm and $D = 2.73 \pm 0.05$ mm, respectively. This prediction slightly overestimates the critical height, primarily due to the approximation of the soap film deformation as a cylinder of length $6R$. In reality, the radius and length of this cylinder vary depending on the crossing velocity and the droplet shape at the moment of impact. Nevertheless, since Eq. 4 provides a first-order dimensional approximation, it is in good agreement with the experimentally determined values.

Note that the thickness of the films is not controlled in these experiments and varies significantly from one trial to another, as stated in the previous section. However, the resulting data fluctuations are sufficiently small to consider, at leading order, the variations in the film thicknesses as negligible. In addition, while it is not con-

Diameter (mm)	Glycerol (wt%)	A_{th} $\left(\mathrm{mm}^{-1}\right)$	A $\left(\mathrm{mm}^{-1}\right)$	B	$-B/A \equiv h_c$ (mm)
2.11 ± 0.01	0	1.61 ± 0.09	1.46 ± 0.01	-51.40 ± 2.04	35.14 ± 1.44
	30	1.67 ± 0.06	1.51 ± 0.06	-58.67 ± 10.95	39.21 ± 5.66
	50	1.74 ± 0.09	1.55 ± 0.07	-63.02 ± 9.35	40.88 ± 4.09
2.73 ± 0.05	0	2.04 ± 0.08	1.87 ± 0.02	-50.19 ± 1.35	26.85 ± 0.79
	30	2.11 ± 0.08	1.90 ± 0.05	-51.72 ± 2.53	27.26 ± 0.73
	50	2.17 ± 0.09	1.99 ± 0.08	-52.58 ± 2.68	27.50 ± 0.70

TABLE II. Theoretical Weber number increase per unit length, A_{th}, and the fitted value from experiments, A. The parameter B quantifies the Weber number loss upon film crossing, and $-B/A$ gives the minimum height for a droplet to cross a soap film. Data are shown for two droplet diameters and three solutions.

sidered in this study, it is likely that the glycerol concentration of glycerol-containing soap films increases in time because of the evaporation of water [31].

In summary, the crossing of a soap film imposes an almost constant energy cost on the droplet. Expressed in terms of the Weber number, this cost satisfies $\Delta\mathrm{We} \in [40, 70]$ and is not significantly influenced by viscosity or droplet size within the investigated ranges.

B. Single encapsulation

Encapsulation by a single soap film has been observed to occur in two distinct speed ranges, corresponding to a low and a high Weber number regime [17–19]. In this section, we present the comparable results we obtained for single encapsulation.

The first regime, the low-speed one, is presented in Fig. 4(a) for $\mathrm{We_{in}} = 62$. The reference time $t = 0\,\mathrm{ms}$ corresponds to the moment the droplet begins interacting with the soap film, *i.e.*, the instant when the bottom of the droplet reaches the same vertical position as the film. Initially, both the droplet and the thin film are deformed ($t = 11.76\,\mathrm{ms}$), then the droplet is pulled upward ($t = 15.29\,\mathrm{ms}$) until the film pinches off ($t = 17.65\,\mathrm{ms}$), leaving behind an encapsulated droplet ($t = 29.41\,\mathrm{ms}$).

The second regime, depicted in Fig. 4(b) for $\mathrm{We_{in}} = 307$, exhibits a slightly different encapsulation process. The soap film undergoes a deformation ($t = 4.11$ ms), stretches, and rapidly pinches off ($t = 6.71$ ms), resulting in an encapsulated droplet with an air pocket at the top.

To characterize the encapsulation behavior by a single soap film, a total of 1275 droplet crossings for the 0 wt% glycerol solution was conducted, covering 17 different release heights and three droplet radii, with 25 trials per height–radius combination. For the 30 wt% and 50 wt% glycerol solutions, the same protocol was applied; however, due to the increased viscosity, the smallest-radius droplets could not be reliably formed using the syringe. Larger needles were tested to reduce flow resistance, but these produced large droplets that broke up the soap film upon crossing. As a result, only two droplet radii could be used for the higher glycerol concentrations, yielding 850 crossing per solution. All droplet crossing were analyzed manually from recorded high-speed videos to accurately determine the occurrence of encapsulation events.

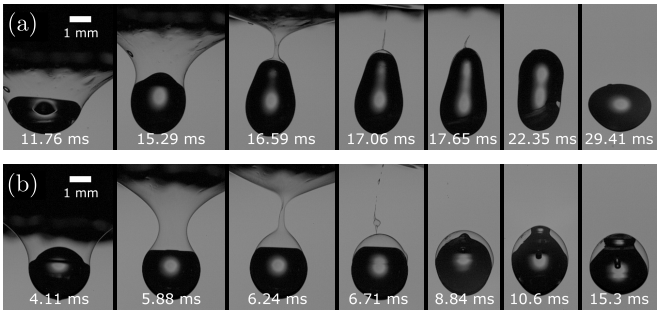

FIG. 4. Image sequences of a droplet with a diameter $D = 2.58\,\mathrm{mm}$ passing through a soap film. The droplet and the film are made from the same solution containing 30 wt% glycerol: (a) low speed regime ($h_{\mathrm{in}} = 29\,\mathrm{mm}, \mathrm{We_{in}} = 62$) and (b) high speed regime ($h_{\mathrm{in}} = 142\,\mathrm{mm}, \mathrm{We_{in}} = 307$). The time $t = 0\,\mathrm{ms}$ corresponds to the moment when the bottom of the droplet reaches the vertical position of the soap film, *i.e.*, when the interaction between the droplet and the film begins.

Although the number of repetitions per considered h_{in} is limited to 25, it is sufficient to extract meaningful statistical trends. Results are presented as the probability of encapsulation as a function of the Weber number and are shown in Fig. 5. The colors and the markers of the data points correspond to different glycerol concentration: 0 wt% (blue bullets), 30 wt% (orange squares), and 50 wt% (green triangles). Error bars represent 95% confidence intervals computed using the Clopper–Pearson method [32], which suits particularly well the experiments due to the sample size and its binary outcome.

To distinguish regions where encapsulation can occur from those where it may result from rare or incidental events, a threshold probability P_c of 0.2 can be defined. This value corresponds to five encapsulations out of 25 trials, which is considered sufficient to suggest a consistent probability of happening rather than stochastic occurrence. Based on this criterion and using the 0 wt% glycerol solution to define the two encapsulation regimes, the low Weber number encapsulation regime spans approximately from $\mathrm{We} \approx 35$ to $\mathrm{We} \approx 85$. The high Weber number regime begins around $\mathrm{We} \approx 170$ and stops

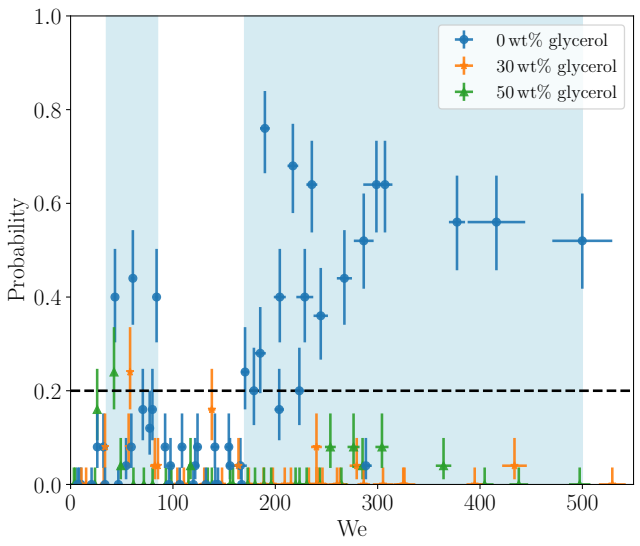

FIG. 5. Probability of droplet encapsulation by a single soap film for three different solutions: 0 wt% glycerol (in blue), 30 wt% glycerol (in orange), and 50 wt% glycerol (in green). The two Weber number ranges in which encapsulation is probable are highlighted in light blue areas. Each point represents the results of 25 trials, and the error bars indicate the 95% confidence intervals computed using the Clopper-Pearson method.

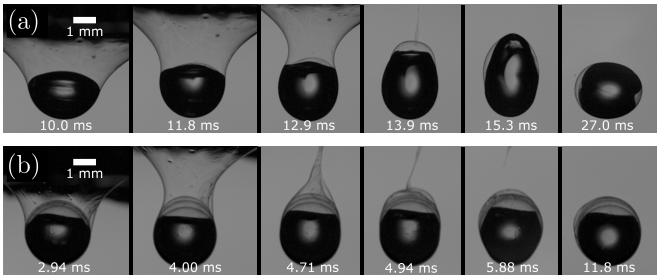

FIG. 6. Image sequences of a droplet of $D = 2.58\,\text{mm}$ passing through the second (a) and fourth (b) soap films. Both the droplet and the films are composed of a solution containing 30 wt% glycerol. The reference time $t = 0\,\text{ms}$ corresponds to the instant when the packed droplet begins to interact with the respective film, defined as the moment when the bottom of the droplet reaches the vertical position of the second (a) or fourth (b) film. (a) The distances are $h_{\text{in}} = 30\,\text{mm}$ and $h_1 = 25\,\text{mm}$, corresponding to Weber numbers $\text{We}_{\text{in}} = 69$ and $\text{We}_1 = 59$. (b) The distances are $h_{\text{in}} = 140\,\text{mm}$, $h_1 = 45\,\text{mm}$ and $h_2 = h_3 = 35\,\text{mm}$, resulting in Weber numbers $\text{We}_{\text{in}} = 293, \text{We}_1 = 311, \text{We}_2 = 307$, and $\text{We}_3 = 304$.

around $\text{We} \approx 500$. These ranges are represented in the Fig. 5 by the two light blue areas. Considering the experimental variations, these two ranges are consistent with those found in literature [17–19].

As expected, if the droplet's speed is too low, meaning the Weber number is significantly below 35, the droplet bounces or coalesces with the soap film upon impact [17]. Conversely, if the droplet's speed is too high and exceeds the low-speed regime but is still below the high-speed regime ($85 < \text{We} < 170$), the soap layer fails to fully cover the droplet or wraps around it before rupturing a few milliseconds later. Although it is not explicitly demonstrated by the Fig. 5, at high Weber numbers ($\text{We} > 500$), the droplet simply passes through the film without being encapsulated or, if the radius is too large, breaks the soap film.

Regarding the effect of viscosity, the two encapsulation ranges observed for the 0 wt% glycerol solution are preserved for the more viscous 30 wt% and 50 wt% glycerol solutions. However, increasing viscosity strongly reduces the probability of encapsulation across the investigated Weber number range. The mean probability decreases from 0.21 for the 0 wt% solution to 0.03 for the more viscous solutions, while the maximum probability drops from 0.76 to 0.24. In addition, the high-Weber number range becomes much narrower, with the probability remaining sufficiently high to rule out random fluctuations, but dropping to around 10%. These results demonstrate that viscosity significantly affects the probability of droplet encapsulation by increasing the viscous damping in the film. When the damping becomes too strong, *i.e.*, the viscosity is sufficiently high, it prevents the droplet from crossing the film. However, with a properly adjusted experimental setup, encapsulation remains moderately probable even at higher viscosities.

To summarize, single encapsulation is most likely to occur within two Weber number ranges, $[35, 85]$ and $[170, 500]$, corresponding to the low- and high-speed regimes, which is in agreement with the existing literature. The low-speed regime is roughly unaffected by an increase of viscosity, although the success rate decreases, while the high speed regime is both much narrower in terms of relevant Weber number range and much less successful within that range for both the tested higher viscosities, as compared to the low viscosity solution

C. Double encapsulation

In principle, it is sufficient to apply the single-encapsulation criterion to an already encapsulated droplet to obtain a second encapsulation. However, since the probability of encapsulation can be lower than 10%, producing multiple encapsulated droplet may be difficult. Moreover, the surface energy of the packed droplet increases after each successful encapsulation by a term $8\pi R^2\gamma$. As a consequence, the droplet becomes less and less deformable, and its interaction with the surrounding air may be altered. These considerations motivate the need to investigate the multiple encapsulation process.

To generate a double-encapsulated droplet, the tip of the syringe is placed at a distance h_{in} from the first soap film. The second soap film is placed at a distance h_1 from the first one, as depicted in Fig. 1.

The double encapsulation process in the low-speed

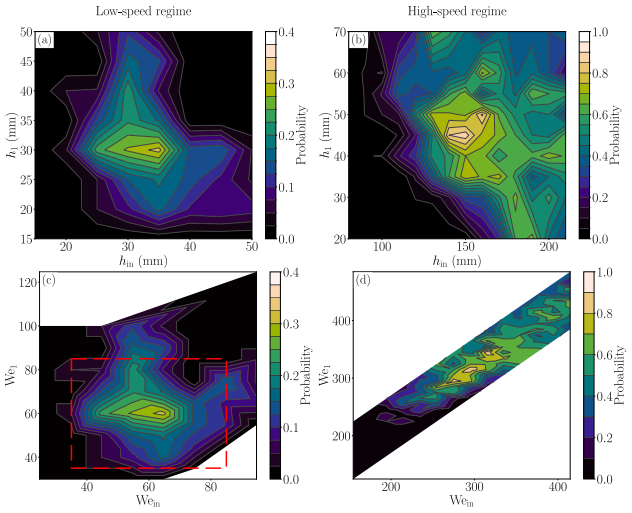

FIG. 7. Probability of achieving double encapsulation for a droplet of $D = 2.64$ mm with a pure solution (0 wt% glycerol) in a (h_{in},h_1)-map (a,b) and the associated (We_{in},We_1)-map (c,d) for low- and high-speed regimes. The red dashed rectangle delimits the working conditions for a single encapsulation with one film in the low-speed regime.

regime is illustrated in Fig. 6(a). The distances used are $h_{in} = 30$ mm and $h_1 = 25$ mm, corresponding to Weber numbers $We_{in} = 69$ and $We_1 = 59$. Similar to the crossing of the first film, the encapsulated droplet is deformed during its passage through the second film. This indicates that despite being encapsulated once, the packed droplet remains deformable. Although quantifying the change in deformability would be interesting, the videos collected during the experiments cover at most a single oscillation period, which does not allow reliable measurements. Estimating deformability under these conditions would be prone to significant error. Therefore, we chose not to include such an analysis in this paper.

Experiments were next conducted using droplets of $D \approx 2.64$ mm and a solution exclusively composed of soap and distilled water. For each set of distances (h_{in}, h_1), between 20 and 30 droplet crossings were analyzed. The soap films were renewed for each set. The probabilities of forming double-encapsulated droplets, *i.e.*, for a droplet to be encapsulated twice, are depicted in Fig. 7, both in the (h_{in}, h_1) space (Fig.7(a,b)) and in the (We_{in}, We_1) space (Fig.7(c,d)). The experimentally measured Weber numbers upon crossing the first (We_{in}) and the second (We_1) soap film are chosen within the regimes in which single encapsulations are most probable, as described in the previous section.

In the low-speed regime, the optimal parameters to obtain a double-encapsulated droplet are $h_{in} = 35$ mm and $h_1 = 30$ mm, corresponding to Weber numbers of $We_{in} = 65$ and $We_1 = 60$, with an approximated success rate of 30 % as depicted in Fig. 7(a,c). The red dashed rectangle delimits the Weber number range required for achieving single encapsulation with one film in the low-speed regime, which is [35, 85]. The good match between the high probability range for single and double encapsulation in the Weber spaces suggests that double encapsulation proceeds from a similar phenomenology as single encapsulation in this interval.

At high falling speeds, the optimal parameters for achieving a double-encapsulated droplet are $h_{in} = 150$ mm and $h_1 = 45$ mm, resulting in a success probability of approximately 80%, as shown in Fig. 7(b). The corresponding Weber numbers are $We_{in} = 295$ and $We_1 = 315$. Clearly, if the droplet speed is too low, *i.e.*, if the Weber numbers are too small ($We_{in} < 200$ or $We_1 < 240$), the double encapsulation can never occur due to the energy being too small to sufficiently deform the soap film. Similarly, if the speed is too high ($We_{in} > 330$ or $We_1 > 360$), the droplet crosses without packing, coalesces or breaks the soap film.

The We_1 values exhibit slight deviations compared to Weber number needed to obtain a single encapsulation, especially in the high-speed regime. This is attributed to the fact that an encapsulated droplet behaves differently than a non-encapsulated one. The presence of the extra layer results in the droplet being more rigid and maintaining a more spherical shape, as evidenced when comparing inner droplet deformation between the sequence depicted in Fig. 4 and those in Fig. 6(a) and (b). Additionally, the trapped air between the layers alters the effective diameter of the droplet, particularly in the high-speed regime, thereby enhancing the influence of surface tension effects during film crossing. Remarkably, the double encapsulation probability is not significantly different to the single encapsulation probability, which means that the second encapsulation is more probable. This suggests that the disruption of the droplet deformation dynamics, caused by the surrounding soap film, is responsible for an increase of the success rate.

To investigate the influence of viscosity on double encapsulation, droplets containing varying percentages of glycerol (0 wt%, 30 wt% and 50 wt%) were employed, along with soap films containing systematically the same amount of glycerol. These droplets had diameters of 2.60 mm, 2.58 mm, and 2.51 mm for the 0 wt%, 30 wt%, and 50 wt% solutions, respectively.

The probability to obtain a double encapsulation as a function of the distances h_{in} and h_1, and Weber numbers We_{in} and We_1, is presented in Fig. 8. For each point on the map, the statistics are based on 20 to 30 droplet crossings, corresponding to approximately 5500 individual experiments in total. For the solution with no glycerol, depicted by Fig. 8(a,d), the optimal parameters are $We_{in} = We_1 = 65$. Whereas, for the 30 % solution, represented in Fig. 8(b,d), these values are $We_{in} = 58, We_1 = 42$, with the same success rate as for the 0 wt% solution and a slightly larger area. However, in the case of the 50 wt% solution (Fig. 8(c,f)), the probability of forming a double-encapsulated droplet is significantly decreased, in the same proportion as for single encapsulation (Fig. 5).

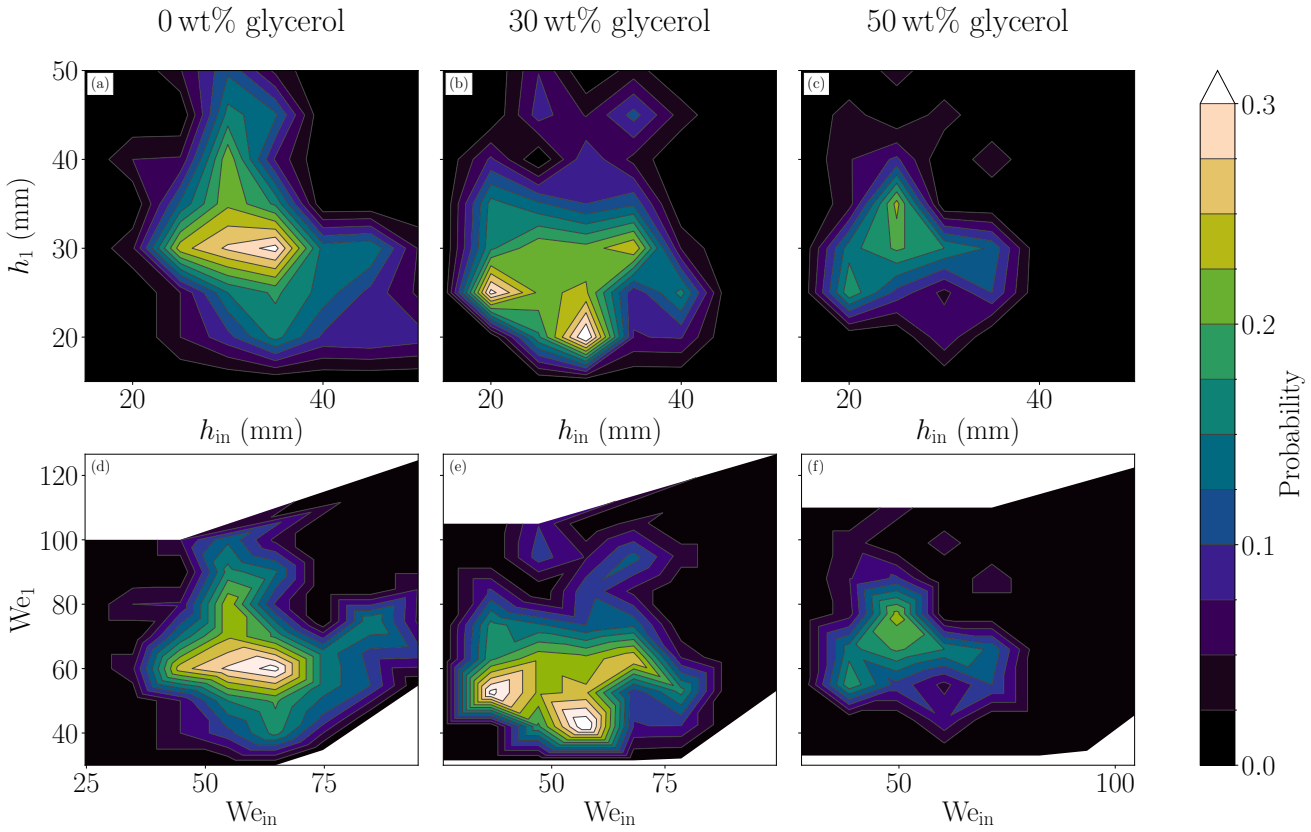

FIG. 8. Probability of achieving double encapsulation for three viscosities in the low-speed regime in a (h_{in},h_1)-map (a,b,c) and in the associated (We_{in},We_1)-map (d,e,f). Note that (a) and (d) are identical to (a) and (c) in Fig. 7.

In summary, double encapsulation in the low Weber regime is essentially following the same rules as single encapsulation: (i) the relevant low Weber range to optimize the process is around 35 - 85 for both films, and (ii) the success rate is weakly affected by viscosity of the 30 wt% glycerol solution. However, for the 50 wt% glycerol solution, the probability decreases sharply. In general, the probabilities for double encapsulation are very similar to those for single encapsulation within experimental fluctuations, suggesting that the first encapsulation and associated increase of surface energy renders the next encapsulation more probable. These findings set the stage for exploring the more complex behavior of multilayer configurations in the following section.

D. Multilayer encapsulation

The encapsulation process can be repeated in order to obtain multilayer packed droplets. However, as additional layers form, the probability of forming a new layer decreases. To ensure successful multilayer encapsulation, the distance between successive soap films must compensate for the kinetic energy lost during each film crossing. To maximize the probability of forming such structures, the following procedure was adopted: (i) the distance h_{in} between the syringe and the soap film is such that the impact Weber number We_{in} corresponds to the previously determined maximum probability of encapsulation; (ii) the successive heights h_i between the successive soap films compensate for the Weber number decrease ΔWe, which comes down to the condition:

$$h_i = \frac{\Delta We}{A_{th}} = \Delta We \frac{\gamma}{2\rho g D} \tag{5}$$

As stated in the Sec. III A, ΔWe typically lies in the range of $[40, 70]$ and does not vary significantly with viscosity. However, it is important to emphasize that while viscosity does not change the Weber number loss, thus the condition for optimal spacing, the viscosity value strongly influences the overall probability of forming multilayer encapsulated droplets, as described in previous sections.

Experiments on droplets encapsulated four times have been successfully conducted. Best results are obtained when the first encapsulation is achieved through a high-speed encapsulation process and with a solution containing 30 wt% of glycerol. To illustrate this process, an image sequence is presented in Fig. 6(b), corresponding to the crossing of the fourth soap film. In this experiment, both the droplet and soap films are made from a solution containing 30 wt% of glycerol. The distances are $h_{in} = 140$ mm, $h_1 = 45$ mm and $h_2 = h_3 = 35$ mm, resulting in

Weber numbers $\mathrm{We_{in}} = 293, \mathrm{We_1} = 311, \mathrm{We_2} = 307$, and $\mathrm{We_3} = 304$. The reference time $t = 0\,\mathrm{ms}$ is defined as the instant when the bottom of the packed droplet reaches the vertical position of the fourth soap film. The presence of the three preexisting layers can be observed at $t = 4.00\,\mathrm{ms}$ and $t = 4.71\,\mathrm{ms}$. The formation of the fourth layer can be seen after the pinch-off at $t = 4.94\,\mathrm{ms}$. The amount of entrapped air between the layers appears much smaller after the first encapsulation, indicating that subsequent layers less significantly affect the effective diameter of the encapsulated droplet.

As stated in the example provided, the encapsulation occurs in the high-speed regime, as it is practically easier to achieve in that regime. Indeed, working in the low-speed regime requires more precise adjustments, since the initial Weber number typically lies in the range of $[35, 85]$, while the loss $\Delta\mathrm{We}$ is around 40 and 70. This leaves a much narrower margin for satisfying the condition required for multilayer encapsulation. Nevertheless, h_1 slightly differs from h_2 and h_3. This discrepancy arises because the optimal film spacings are defined as ranges, not fixed values. In practice, we aim to remain within the appropriate Weber number intervals to maximize the probability of successive encapsulations. Given the experimental nature of this work, such deviations from ideal theoretical values are to be expected, particularly since the soap film thicknesses are not controlled.

To summarize, multilayer encapsulation can be achieved by first setting $\mathrm{We_{in}}$ within the optimal range for encapsulation, corresponding to $[35, 85]$ in the low-speed regime and $[170, 500]$ in the high-speed regime, and then choosing successive film spacings according to Eq. 5, with $\Delta\mathrm{We} \in [40, 70]$. These conditions provide a practical guideline for designing successful multilayer encapsulation experiments.

E. Antibubble formation

Generating a single- and multi-layer antibubbles using one or multiple soap film is relatively straightforward. A droplet of soapy liquid passes through N soap films ($N = 1, 2, \dots$), encapsulating it N times, with each layer separated by a thin layer of air. Upon impact with a pool of a 5 wt.% soap-water solution, the outermost soap film merges with the bath, acting as a sacrificial layer. This leaves a droplet encapsulated by N air layers and $N - 1$ inner soap films beneath the pool surface, thus forming a N-layered antibubble [17, 20]. The Supplemental Material [33] shows the formation of a single-layer antibubble (delayed coalescence [34, 35]).

The case of a single encapsulation, where the droplet is wrapped by only one layer of soap film, is illustrated in Fig. 9. The packed droplet has an effective diameter of $D = 3.36\,\mathrm{mm}$, the distance between the needle and the soap film is $h_{\mathrm{in}} = 30\,\mathrm{mm}$ and the distance between the film and the surface of the pool is $h_{\mathrm{pool}} = 20\,\mathrm{mm}$. The associated Weber numbers, measured experimentally before crossing and impacts, are $\mathrm{We_{in}} = 76$ and $\mathrm{We_{pool}} = 71$, respectively. The encapsulated droplet impacts the bath at $t = 0\,\mathrm{ms}$. Following this impact, the outermost liquid layer merges with the bath at $t = 2.5\,\mathrm{ms}$, leaving only the air film and the liquid core. This process generates an antibubble, visible at times $t \geqslant 5.6\,\mathrm{ms}$. Before the stabilization into a spherical shape, we observe that the antibubble is first extremely deformed ($t \geqslant 5.6\,\mathrm{ms}$) and then oscillates. By using this process, the resulting antibubbles have, at leading order, the same diameter as their associated droplets since it is only wrapped by a micro-metric air film.

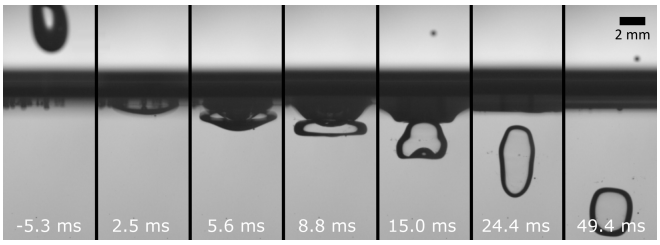

FIG. 9. Image sequence of the formation of an antibubble with a solution of 0 wt% glycerol. The droplet, with an effective diameter of $D = 3.36\,\mathrm{mm}$, is encapsulated by a single soap film before entering a pool made from the same glycerol-free solution. The reference time $t = 0\,\mathrm{ms}$ corresponds to the moment the droplet impacts the bath surface. The spacing between the needle tip and the soap film is $h_{\mathrm{in}} = 30\,\mathrm{mm}$ ($\mathrm{We_{in}} = 76$), and the distance between the film and the pool is $h_{\mathrm{pool}} = 20\,\mathrm{mm}$ ($\mathrm{We_{pool}} = 71$).

The probability of generating an antibubble using this technique, in the case of a single soap film in the low-speed regime, was investigated. Droplets of diameters $D = 2.64\,\mathrm{mm}, 2.58\,\mathrm{mm}$, and $2.51\,\mathrm{mm}$ were used for the 0 wt%, 30 wt%, and 50 wt% solutions, respectively, both for the droplet and the soap film. The pool, however, contained only the solution made from soap and water. The results are presented in Fig. 10, where each point corresponds to one of the eight values of h_{in} combined with one of the eleven values of h_{pool}, yielding a total of 5650 experiments.

For the 0 wt% glycerol solution, generating antibubbles proved to be challenging, with very few antibubbles observed and a maximum probability of 0.08. In contrast, for more viscous solutions containing 30 wt% and 50 wt% glycerol, the maximum probability increased to 0.24. This indicates that viscosity can significantly enhance the probability of generating antibubble using the soap-film method. This viscosity-dependent effect can be attributed to two main phenomena: (i) the damping of oscillations induced by the interaction with the soap films and/or with the bath, and (ii) the viscosity dependence of coalescence dynamics. Regarding the first, it has been shown that a non-spherical droplet impacting a liquid pool modifies the cavity geometry [36]. This implies that the droplet shape, prolate or oblate, affects the coalescence of the outermost soap layer through variations in

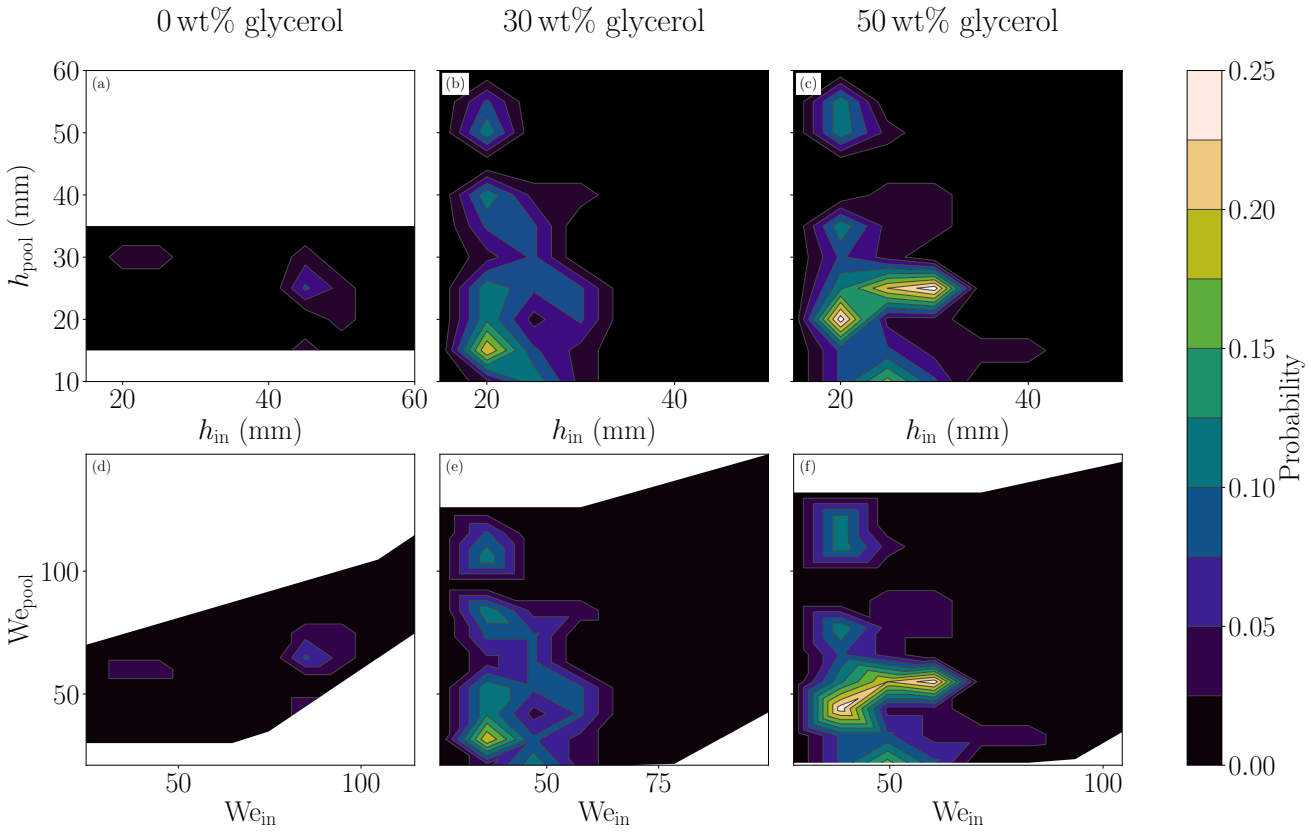

FIG. 10. Probabilities of achieving antibubbles for three viscosities in the low-speed regime in a (h_{in},h_{pool})-map (a,b,c) and in the associated ($\mathrm{We}_{\mathrm{in}}$,$\mathrm{We}_{\mathrm{pool}}$)-map (d,e,f)

the contact area. The damping rate of these oscillations, enhanced by viscosity and scaling as $\sim \rho D^2/(5\mu)$ [37], allows the droplet to recover a nearly spherical shape before impact, thereby improving repeatability and robustness. In addition, the capillary waves generated upon the impact can squeeze the intervening air film and lead to its rupture. Increasing the viscosity damps these waves, thus reducing the likelihood of air-film squeezing. For the second effect, increasing viscosity slows air film drainage and delays coalescence, indeed, the boundary condition for the continuity of the viscous stress on the liquid-gas interface provides a criterion for which the liquid-side stress can be neglected and reads $\mu_{\mathrm{air}}/\mu \gg 2\epsilon/D$ [8], where $\epsilon \sim 3\,\mu$m is the gas film thickness and μ_{air} is the dynamic viscosity of the gas. In our case, this condition is valid for the pure soap solution but not for the solution containing glycerol, which may contribute to (i) the propensity to entrain a thicker air film for a higher droplet viscosity, (ii) a slower air film drainage. Both phenomena lead to thicker air films, therefore less likely to burst before the pinch-off and subsequent antibubble formation.

The number of layers in a multilayer antibubble cannot be directly observed because the total reflection hides its internal structure. However, the layers become visible when the antibubble pops, as they usually rupture at different times. The Supplemental Material [33] shows examples of antibubbles formed with one, two, and three soap films. The order of popping is not controlled. In these videos, both the soap films and the droplets were made from the same water-soap solution.

In summary, generating antibubbles in a soap-water bath using the soap film method is challenging when the solution contains only water and soap. Using more viscous solutions for both the soap films and the droplets increases the probability of antibubble formation, as higher viscosity enhances the conditions for controlled coalescence of the outermost soap film with the liquid bath. It should be noted that while the probability of encapsulation is the highest at larger impact speeds, such conditions are unfavorable for antibubble creation. The encapsulated droplet must contact the bath surface at a sufficiently low speed to allow smooth coalescence of the sacrificial soap layer with the bath.

F. Antibubble lifetime

Since antibubbles are, by nature, not stable, their lifetime is mainly governed by the drainage of the air layer, assuming gas dissolution is negligible over the short timescales considered. Due to the lack of repulsive forces

between the two gas–liquid interfaces, antibubbles ultimately collapse as the gas layer becomes too thin and van der Waals forces dominates [38].

For multilayer antibubbles, several characteristic lifetimes must be considered. In our case, we assume that the intervening soap films between successive air layers remain stable, as no rupture of the inner film was observed over the experiments; hence, only the drainage of the air layers is relevant. This drainage is primarily driven by the hydrostatic pressure gradient between the bottom and the top of the antibubble. In addition, the surface rheology of the interfaces must be accounted for, as it strongly influences the lifetime [8]. For a commercial product such as the one used in this study, the interfaces can be considered incompressible, which means that the surface velocity must be zero because of the spherical geometry of the system [39, 40]. However, since the liquid within the soap films drains in the opposite direction to the air, liquid drainage may also influence the air drainage dynamics in multilayer antibubbles. As this manuscript is intended as a first case study, these aspects are not discussed further here.

Experiments to quantify the lifetime of multilayer antibubbles were carried out using the 50 wt% glycerol solution, for which the probability of antibubble formation is the highest. Droplets of diameters $D = 2.63 \pm 0.05$ mm were used and the distances between the needle, the soap film(s) and the pool have been chosen based on Figs. 8 and 10. For single-layer antibubbles, the distance between the needle and the film was set to $h_{\text{in}} = 20.5 \pm 0.5$ mm ($\text{We}_{\text{in}} \approx 35$) and the one between the film and the pool, to $h_{\text{pool}} = 19.5 \pm 0.5$ mm ($\text{We}_{\text{pool}} \approx 28$). For the two-layers case, we set $h_{\text{in}} = 20.5 \pm 0.5$ mm ($\text{We}_{\text{in}} \approx 35$), $h_1 = 30 \pm 0.5$ mm ($\text{We}_1 \approx 45$), and $h_{\text{pool}} = 19.5 \pm 0.5$ mm ($\text{We}_{\text{pool}} \approx 28$). The lifetimes were recorded at 100 fps using a high-speed camera. Both single-layer and two-layers antibubbles were generated, and their lifetimes τ were analyzed using the Cumulative Distribution Functions (CDFs). As the process is a death-type phenomenon, a Weibull distribution is appropriate to describe the data. The CDF of the Weibull distribution is given by

$$F(\tau) = \begin{cases} 1 - e^{-(\tau/\lambda)^k} & , \quad \tau \geqslant 0 \\ 0 & , \quad \tau < 0 \end{cases} \tag{6}$$

where λ is the scale parameter and k, the shape parameter. The results are presented in Fig. 11(a) for both single-layer (orange dots) and two-layers (blue stars and dots) antibubbles.

A total of 102 antibubbles were analyzed to obtain the CDF of the lifetime τ_1 of single-layer antibubbles. The lifetime distribution follows a Weibull law with a shape parameter $k_1 = 1.02$ and a scale parameter $\lambda_1 = 14.88$ s, consistent with an exponential (Markovian) process, as reported in previous studies [41]. This indicates that the rupture probability is constant in time and caused by random events such as the presence of dust particles in the air layer or microbubbles. The mean lifetime is $\bar{\tau}_1 = 15.45 \pm 16.02$ s, about seven times shorter than typical literature values [8, 41, 42]. It is worth noting that the air volume of each layer was not controlled in these experiments.

For two-layers antibubbles, two distinct lifetimes can be measured: the outer gas layer lifetime $\tau_{2,\text{o}}$ and the inner gas layer lifetime $\tau_{2,\text{i}}$. The external and internal collapses are identified from the position of the bubbles that remain after rupture. If the resulting bubbles are visible in the bath, the outer layer has collapsed; if no bubbles are observed in the bath, the inner layer has collapsed. The lifetimes were analyzed separately and depicted by blue stars and blue dots on Fig. 11(a), respectively. In all experiments, we observed that the outer layer was the first one to burst and, therefore, the overall lifetime τ_2 of two-layers antibubbles is such that $\tau_2 = \tau_{2,\text{i}}$. A total of 88 two-layers antibubbles were analyzed to obtain the corresponding CDFs. We often observed that the outer layer ruptured immediately after the coalescence of the outermost soap film with the bath. Including direct ruptures upon impact, the mean outer-layer lifetime is $\bar{\tau}_{2,\text{o}} = 0.38 \pm 1.28$ s. By fitting a Weibull law, the shape parameter of the distribution is $k_{2,\text{o}} = 0.15$ and the scale parameter $\lambda_{2,\text{o}} = 2.58 \cdot 10^{-3}$ s, indicating that the bursting probability is high immediately after formation and decreases with time, as observed experimentally. For the inner layer, the mean lifetime is $\bar{\tau}_{2,\text{i}} = 7.67 \pm 8.96$ s, with a shape factor $k_{2,\text{i}} = 0.76$ and a scale parameter $\lambda_{2,\text{i}} = 6.81$ s, intermediate between early failure and a Markovian process. This suggests that the collapse of the outer layer destabilizes the inner one, as it was observed during experiments.

The analysis was repeated after excluding cases where the outer layer ruptured during merging, which represents a smaller sample of 19 events, as presented in Fig. 11(b). Even within this reduced dataset, the outer layer remains the first to collapse. When both distributions are fitted with a Weibull law, a Markovian behavior ($k_{2,\text{i}} = 0.92 \approx 1$, $\lambda_{2,\text{i}} = 4$ s) is recovered for the inner layer. However, the mean inner-layer lifetime $\bar{\tau}_{2,\text{i}} = 4.68 \pm 5.25$ s remains about three times shorter than that of single-layer antibubbles, confirming the lower overall stability of multilayer structures. For the outer layer, a shape parameter of $k_{2,\text{o}} = 0.50$ ($\lambda_{2,\text{o}} = 0.73$ s) is obtained, indicating that even when the outer layer survives the merging process, it remains highly unstable and subject to early collapse.

In addition, as presented in Fig. 11(c), the CDF of the inner layer is reported again, but the corresponding outer layer lifetimes are sorted to underline the possible correlation between the rupture of the outer layer and the inner one. For short lifetimes, *i.e.* shorter than 2 s, the inner and outer layer rupture at almost the same time ($\tau_2 \approx \tau_{2,\text{i}} \approx \tau_{2,\text{o}}$). For longer lifetimes, *i.e.* when $\tau_2 > 2$ s, the bursting of both the outer and inner layer are less correlated. This trend is consistent with shape parameters closer to one (Markovian process) found for

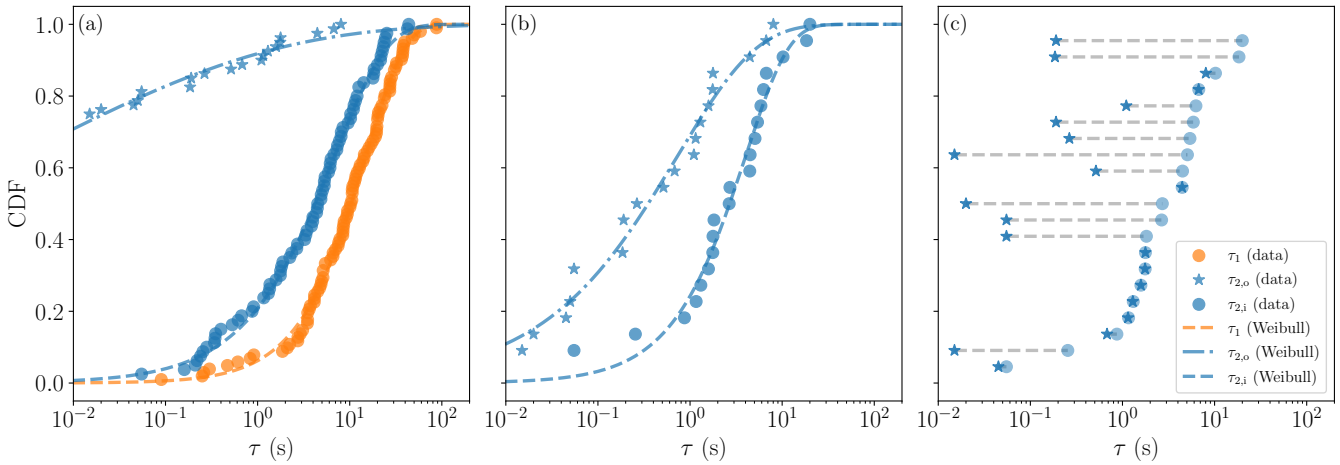

FIG. 11. (a) Cumulative Distribution Functions (CDFs) of the lifetimes of one-layer (orange) and two-layers (blue) antibubbles. For two-layers antibubbles, stars represent the lifetime of the outer layer, while dots represent that of the inner layer. Dashed and dash-dotted lines represent the corresponding Weibull fits. (b) CDFs of two-layers antibubbles after removing cases where the outer layer collapsed upon impact with the bath. Dashed and dash-dotted lines show the Weibull fits. (c) CDFs of two-layers antibubbles showing both outer (stars) and inner (dots) layers, with the outer-layer data sorted to correspond to each inner-layer measurement.

the CDFs of both layers when the data is 'cleaned'.

To summarize, the lifetime of two-layers antibubbles is equal to the lifetime of the innermost gas layer. The collapse of the outer gas layer is most often observed upon impact. When the outer layer survives the impact phase and bursts within the next two seconds, it is positively correlated to the early collapse of the inner layer, while this is not true anymore after two seconds. This last observation is based on a low sample size and may therefore be biased.

These results provide the first quantitative comparison of antibubble lifetimes obtained via multilayer encapsulation. While multilayer antibubbles can be generated reliably, their stability is reduced compared to single-layer antibubbles, primarily due to the fragility of the outer shell and, secondarily, to interlayer interactions.

IV. CONCLUSION

In this paper, we have investigated the encapsulation of droplets by one or multiple soap films. Single and double encapsulations are most probable within two Weber-number ranges, We $\in [35, 85]$ and We $\in [170, 500]$, defining two velocity regimes. Low viscosities do not significantly affect the encapsulation probability in the low-speed regime, whereas higher viscosities strongly reduce it in the high-speed regime for single encapsulation and in the low-speed regime for double encapsulations. By appropriately spacing successive films, up to four successive encapsulations were achieved, demonstrating the robustness of the method.

In addition, a method to generate single- and double-layer antibubbles was presented. Increases in viscosity were found to increase the probability of single-layer antibubble formation by roughly a factor of six. Stability studies showed that multilayer antibubbles are less stable than single-layer ones, with outer layers systematically bursting first, and that single-layer antibubbles created via the soap-film method have shorter lifetimes than those generated by direct jet impact [8]. These results constitute the first experimental investigation of multilayer antibubble stability and provide quantitative guidelines for their reproducible formation.

Compared with existing techniques, the submerged bell allows precise control over air and liquid volumes but requires gas and liquid inlets [8], while the pouring method produces larger antibubbles with uncontrolled size and air content [7]. The soap-film method provides an intermediate alternative: it is simple, allows tuning of antibubble size via the needle radius, and achieves a practical balance between simplicity and reproducibility. This approach holds potential for controlled mass production of single- and multilayer antibubbles.

ACKNOWLEDGMENTS

The authors thank Antoine Debuigne for the use of the pendant drop tensiometer. This work was supported by the Fonds de la Recherche Scientifique (F.R.S.-FNRS) under research project STAB-AB (PDR T.0204.23). S. Dorbolo is a Senior Research Associate at F.R.S.-FNRS, and B. Scheid is a Research Director at F.R.S.-FNRS.

[1] W. Hughes and A. R. Hughes, Nature **129**, 59 (1932), number: 3245 Publisher: Nature Publishing Group.
[2] S. Pavlov-Verevkin, Khimiya i Zhizn' [Chemistry and Life] **11**, 12 (1966).
[3] S. Kotopoulis, K. Johansen, O. Gilja, A. Poortinga, and M. Postema, Acta Physica Polonica A **127**, 99 (2015).
[4] J. E. Silpe and D. W. McGrail, Journal of Applied Physics **113**, 17B304 (2013).
[5] J. Miguet, S. Dorbolo, and B. Scheid, Chemical Engineering Journal **498**, 153276 (2024).
[6] R. Zia, A. Nazir, A. T. Poortinga, and C. F. van Nostrum, Advances in Colloid and Interface Science **305**, 102688 (2022).
[7] S. Dorbolo, H. Caps, and N. Vandewalle, New Journal of Physics **5**, 161 (2003).
[8] Y. Vitry, S. Dorbolo, J. Vermant, and B. Scheid, Colloids and Surfaces A: Physicochemical and Engineering Aspects **270**, 73 (2019).
[9] W. Suhr, European Journal of Physics **33**, 443 (2012).
[10] P. G. Kim and H. A. Stone, Europhysics Letters **83**, 54001 (2008).
[11] A. Tufaile and J. C. Sartorelli, Physical Review E **66**, 056204 (2002).
[12] A. T. Poortinga, Colloids and Surfaces A: Physicochemical and Engineering Aspects **419**, 15 (2013).
[13] S. T. Thoroddsen, K. Takehara, T. G. Etoh, and Y. Hatsuki, Journal of Fluid Mechanics **530**, 295 (2005), publisher: Cambridge University Press.
[14] L. Courbin and H. A. Stone, Physics of Fluids **18**, 091105 (2006), publisher: American Institute of Physics.
[15] S. T. Thoroddsen, T. G. Etoh, and K. Takehara, Physics of Fluids **19**, 052101 (2007).
[16] T. Gilet and J. W. M. Bush, Journal of Fluid Mechanics **625**, 167 (2009), publisher: Cambridge University Press.
[17] J. Zou, W. Wang, C. Ji, and M. Pan, Physics of Fluids **29**, 062110 (2017), publisher: American Institute of Physics.
[18] Y. Ya-Jing, M. Chen-Xi, Z. Xu-Dong, W. Yan-Ju, and L. Sheng-Hua, Acta Physica Sinica **68**, 156101 (2019).
[19] Y. Wei, Z. Mu, Y. Zhang, Y. Yang, S. Liu, C. K. Law, and A. Saha, Journal of Fluid Mechanics **933**, A32 (2022), publisher: Cambridge University Press.
[20] L. Bai, W. Xu, P. Wu, W. Lin, C. Li, and D. Xu, Colloids and Surfaces A: Physicochemical and Engineering Aspects **509**, 334 (2016).
[21] L. Bai, J. Sun, Z. Zeng, Y. Ma, and L. Bai, Technical Sciences **23**, 91 (2020).
[22] A. Le Goff, L. Courbin, H. A. Stone, and D. Quéré, EPL **84** (2008), 10.1209/0295-5075/84/36001.
[23] Dreft Original, Technical Data Sheet, Procter&Gamble (2018).
[24] D. S. Ambwani and T. Fort, "Pendant drop technique for measuring liquid boundary tensions," in Surface and Colloid Science: Volume 11: Experimental Methods, edited by R. J. Good and R. R. Stromberg (Springer US, Boston, MA, 1979) pp. 93–119.
[25] (), see Supplemental Material at [URL] for the surface tension curve of Dreft, determined using the pendant drop method.
[26] N.-S. Cheng, Industrial and Engineering Chemistry Research **47**, 3285 (2008).
[27] F. E. C. Culick, Journal of Applied Physics **31**, 1128-1129 (1960).
[28] V. Sanjay, U. Sen, P. Kant, and D. Lohse, Journal of Fluid Mechanics **948**, A14 (2022).
[29] S. T. Thoroddsen, M.-J. Thoraval, K. Takehara, and T. G. Etoh, Journal of Fluid Mechanics **708**, 469 (2012), publisher: Cambridge University Press.
[30] E. Reyssat and D. Quéré, Europhysics Letters (EPL) **76**, 236 (2006).
[31] F. m. c. Boulogne, F. Restagno, and E. Rio, Phys. Rev. Lett. **129**, 268001 (2022).
[32] C. Clopper and E. Pearson, Biometrika **26**, 404 (1934).
[33] (), see Supplemental Material at [URL] for videos of antibubble generation and multilayer antibubble rupture.
[34] T. Gilet, K. Mulleners, J. P. Lecomte, N. Vandewalle, and S. Dorbolo, Phys. Rev. E **75**, 036303 (2007).
[35] G. Pucci, D. M. Harris, and J. W. M. Bush, Physics of Fluids **27**, 061704 (2015).
[36] S. Dighe, D. K. Maity, J. N. Fonnesbeck, S. Dutta, and T. Truscott, **109**, 045107.
[37] A. Aalilija, C.-A. Gandin, and E. Hachem, Computers Fluids **197**, 104362 (2020).
[38] S. Dorbolo, E. Reyssat, N. Vandewalle, and D. Quéré, Europhys. Lett. **69**, 966 (2005).
[39] I. Cantat, S. Pertant, C. Raufaste, and E. Rio, Annual Review of Fluid Mechanics **58**, 111 (2026).
[40] H. Manikantan and T. M. Squires, Journal of Fluid Mechanics **892**, P1 (2020).
[41] S. Dorbolo, D. Terwagne, R. Delhalle, J. Dujardin, N. Huet, N. Vandewalle, and N. Denkov, Colloids and Surfaces A: Physicochemical and Engineering Aspects 4th International Workshop, **365**, 43 (2010).
[42] B. Scheid, J. Zawala, and S. Dorbolo, Soft Matter **10**, 7096 (2014).